iScience

CellPress
OPEN ACCESS

Article

Porous TiO_2 thin film-based photocatalytic windows for an enhanced operation of optofluidic microreactors in CO_2 conversion

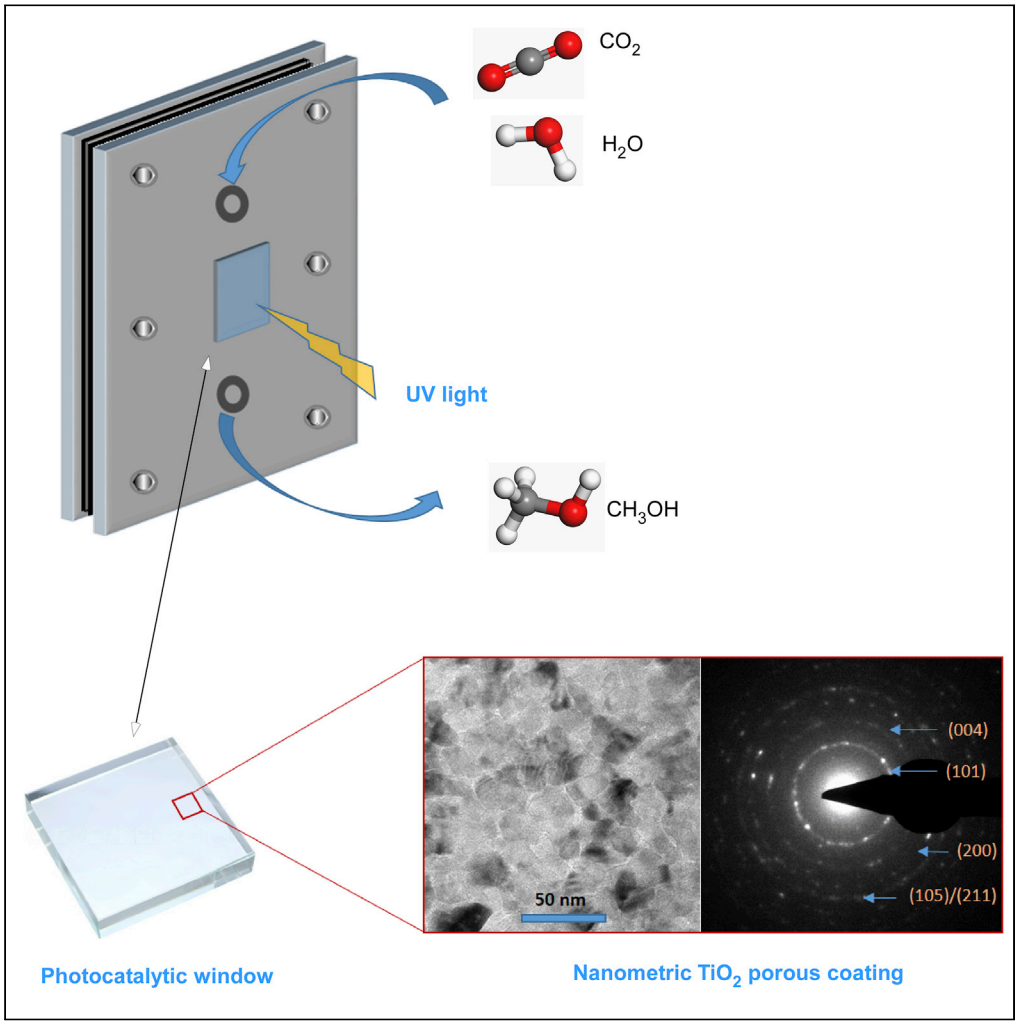

Adrián Angulo-Ibáñez, Amaia M. Goitandia, Jonathan Albo, Estibaliz Aranzabe, Garikoitz Beobide, Oscar Castillo, Sonia Pérez-Yáñez

jonathan.albo@unican.es (J.A.)
garikoitz.beobide@ehu.eus (G.B.)

Highlights

Photocatalytic windows provide enhanced operation of optofluidic microreactors

Use of TiO_2 nanometric coatings reduces the required photocatalyst amount

The robustness of the coating implies stability upon long-working periods

CO_2-to-CH_3OH conversion performance is related to the porosity and crystallite size

Angulo-Ibáñez et al., iScience 24, 102654
June 25, 2021
https://doi.org/10.1016/j.isci.2021.102654

iScience

CellPress
OPEN ACCESS

Article

Porous TiO_2 thin film-based photocatalytic windows for an enhanced operation of optofluidic microreactors in CO_2 conversion

Adrián Angulo-Ibáñez,[1] Amaia M. Goitandia,[1] Jonathan Albo,[2,*] Estibaliz Aranzabe,[1] Garikoitz Beobide,[3,4,5,*] Oscar Castillo,[3,4] and Sonia Pérez-Yáñez[3,4]

SUMMARY

Using a photocatalytic window can simplify the design of an optofluidic microreactor, providing also a more straightforward operation. Therefore, the development of TiO_2 coatings on glass substrates seems appealing, although *a priori* they would imply a reduced accessible area compared with supported nanoparticle systems. Considering this potential drawback, we have developed an endurable photocatalytic window consisting on an inner protective SiO_2 layer and an outer mesoporous anatase layer with enhanced surface area and nanoscopic crystallite size (9–16 nm) supported on a glass substrate. The designed photocatalytic windows are active in the CO_2-to-methanol photocatalytic transformation, with maximum methanol yield (0.52 $\mu mol \cdot h^{-1} \cdot cm^{-2}$) for greatest porosity values and minimum crystallite size. Compared with benchmark supported nanoparticle systems, the nanoscopic thickness of the coatings allowed to save photoactive material using only 11–22 $\mu g \cdot cm^{-2}$, while its robustness prevented the leaching of active material, thus avoiding the decay of performance at long working periods.

INTRODUCTION

A few different laboratory-type photoreactor designs have been assayed for the photocatalytic reduction of CO_2, where slurry reactors with suspended TiO_2 particles are commonly reported (Ola and Maroto-Valer, 2015). This simple configuration, however, has been demonstrated to be inefficient to induce the challenging CO_2 reduction reaction, mainly due to particle agglomeration and poor light utilization efficiency (Ola et al., 2012). Besides this, the separation of the photocatalysts from reaction products at reactor outlet limits the efficiency and economy of the process. Therefore, attention has turned to immobilization of TiO_2 on a substrate to eliminate the need for a follow-up clarifier technique. There are, however, two main drawbacks usually found in these fixed-bed type reactors, namely low specific active area available and material stability. The former issue can be solved using optofluidic microreactors. This microreactor configuration has been demonstrated to bring several advantages, including large surface-area-to-volume ratio, uniform light distribution, enhanced mass transfer, and fine flow control, in contrast to sludge reactors (Wang et al., 2014). In spite of this, their application in the challenging CO_2-to-methanol reaction is still scarce (Albo and García. 2021; Cheng et al., 2017a, 2017b, 2019; Chen et al., 2017). Moreover, the stability issue with longer periods of light irradiation is usually attributed to the reduction in the ability to absorb light due to particle detachment and the formation of intermediate un-desorbed products that block the active sites (Albo et al., 2021). These drawbacks can be overcome by the use of a gauzy reactor vessels or windows whose inner wall is coated by a chemically and mechanically robust film of the photoactive material (Shan et al., 2010; Dijkstra et al., 2001). Such disposition can avoid material detachment and chemical or photochemical degradation during the reaction, but also it would allow a handy regeneration of the material if un-desorbed species remain, by a post-reaction chemical or thermal treatment of the re-assemblable window. Despite this kind of photoactive windows or reactor vessel have been intensively explored, for instance, in tube reactors for water treatment (Khalaf et al., 2019), the examples implying optofluidic microreactors are limited to handful of works (Li et al., 2018) since in this kind of reactors the immobilization of the catalyst is usually provided by a support different to the window (Sohrabi et al., 2020). Furthermore, none of the published works on optofluidic microreactors based on photocatalytic windows deals with their application in the continuous photoconversion of CO_2 to methanol.

[1]Surface Chemistry & Nanotechnologies Unit, Fdn Tekniker, Inaki Goenaga 5, Eibar 20600, Spain

[2]Department of Chemical & Biomolecular Engineering, University of Cantabria, Avda. Los Castros s/n, 39005 Santander, Spain

[3]Departament of Inorganic Chemistry, Faculty of Science and Technology, University of the Basque Country (UPV/EHU), Leioa 48940, Spain

[4]Basque Ctr Mat Applicat & Nanostruct, BCMat, UPV EHU Sci Pk, Leioa 48940, Spain

[5]Lead contact

*Correspondence: jonathan.albo@unican.es (J.A.), garikoitz.beobide@ehu.eus (G.B.)

https://doi.org/10.1016/j.isci.2021.102654

Table 1. Coating codes and corresponding surfactant amount

Code[a]	ALS ratio	ALS mass (%)
PPC-0	0	0
PPC-5	0.02	5
PPC-10	0.04	10
PPC-20	0.07	20
PPC-30	0.11	30

[a]PPC refer to porous photocatalytic coatings while the following number indicates the ALS mass percentage. The ALS molar ratio is set respect TNBT, while the ALS mass implies the total surfactant mass percentage in the sol.

Herein, we developed and assembled into a microreactor a series of photocatalytic windows functionalized with nanometric coatings of TiO_2 (anatase) of controlled crystallite size, porosity, and thickness. The performance figures of CO_2 photoreduction into methanol are related to the microstructural features of the photoactive coatings and collated with the results provided by the alternative supported systems of nanoparticles. At this point, it must be emphasized that usually the windows of this kind of photoreactors consist of substrates such as quartz or borosilicate glass. However, herein we selected common soda-lime glass as it cheapens the device and it eases its potential utilization. It must be noted that the growth of TiO_2 films into soda-lime glass can favor the diffusion of sodium which in turn induce a decay of photocatalytic activity due to the formation of sodium titanates (Fujishima and Rao, 1997), formation of recombination centers (Paz et al., 1995), suppressed crystallization (Lee and Lee, 2007), and particle size increase (Nam et al., 2004). To overcome this problem the glass windows were precoated with an intermediate SiO_2 layer which has demonstrated to inhibit the sodium diffusion into the photocatalytic layer (Novotna et al., 2010). Apart from that, in this work, the interferential maximum provided by the SiO_2 layer is shifted to the absorption edge of TiO_2 to compensate the decay in transmittance of common glass in comparison to low UV-absorbing substrates (quartz or borosilicate glass).

RESULTS AND DISCUSSION

Preparation of photocatalytic windows

All coatings were deposited on soda-lime glass substrates by dip-coating method into inorganic sols. Prior to the deposition of the photocatalytic films, the glass substrates were coated with a protective layer of silicon dioxide, since it improves the UV transmittance and prevents the deactivation ascribed to the migration of alkali or alkali earths from glass, allowing as consequence using common glass as substrate instead of alkali free borosilicate glass or quartz. The photocatalytic coatings were prepared varying the amount of surfactant in order to control the porosity and crystallite size. Table 1 gathers the codes for the photocatalytic coatings together with the corresponding surfactant amount. Further details on the preparation of the coatings are provided in the experimental procedures.

Characterization of the photocatalyst films

According to the profile matching analysis performed on the PXRD patterns (Figure 1 and Table S1), selected heat treatment conditions were suitable to render anatase as the main crystalline phase. No traces of rutile were observed on the diffractograms.

Interestingly, the increase of the amount of surfactant in the sol formulation leads to a widening of the peaks (Figure 2 and Figure S2) which can be related to a size reduction of the crystalline domains. Note that crystallite (particle) size can dominate both photocatalytic activity and reaction kinetic. Table 2 shows the full width at half maximum (FWHM) for the reflection (101) and the crystallite size (D_{hkl}) calculated from Scherrer equation (see supplemental information) (Klug and Alexander, 1974; Holzwarth and Gibson, 2011).

All coatings present nanoscopic crystallites. Greatest ones (*ca.* 16 nm) are found for PPC-0 and tend to stabilize around 10 nm for PPC-20 and PPC-30. In fact, incorporation to the sols of greater amounts of ALS did not allow us to reduce further the crystallite size.

TEM images collected on exfoliated lamellas (Figure 3) reveal that the coatings consist of intimately sinterized crystallites. The size estimated (17(3) and 10(3) nm for PPC-0 and PPC-20, respectively) fit well to those subtracted from the PXRD analysis. The sinterisation among the crystallite render interstitial nanometric voids that lie within the lower limit of mesopore regime (see below).

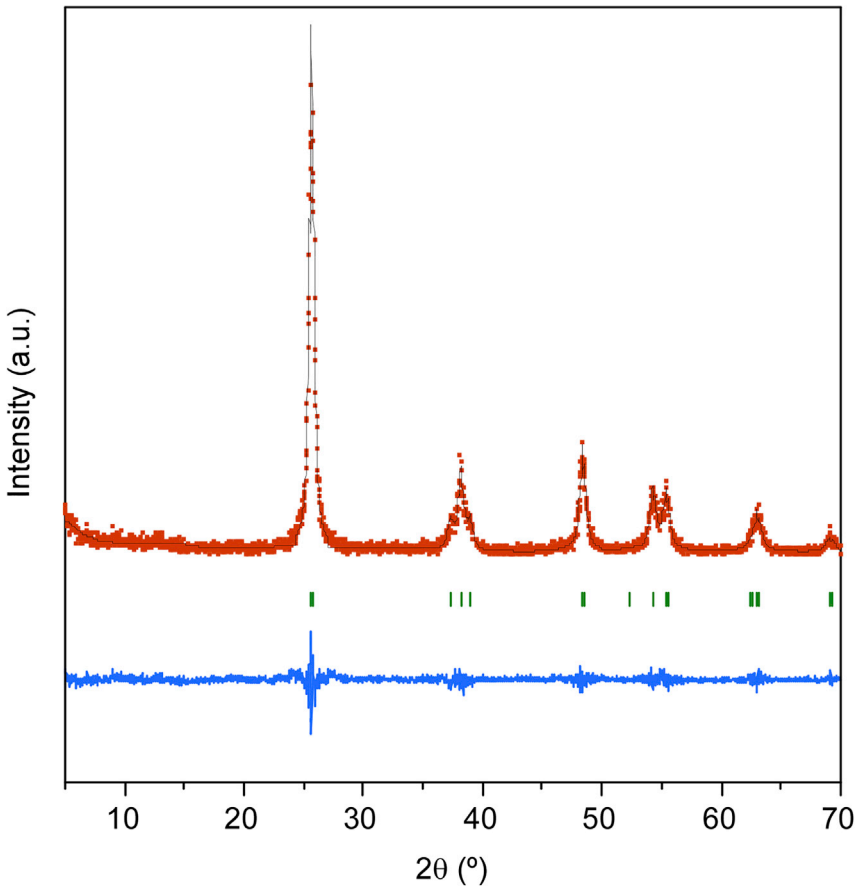

Figure 1. Plot of the profile matching analysis performed on PXRD pattern of PPC-0
Red dots: experimental pattern; black line: calculated pattern; blue line: difference; green ticks: calculated reflections. The profile fitting was performed on the basis of the crystal structure parameters of anatase (ICSD no.: 024276).

The selected area electron diffraction (SAED) plots show ring patterns attributable to a lamella comprised by ultrafine grains of polycrystalline materials (inset graphic of Figure 3). Measured spacing values are consistent with the Miller indices of anatase. Details of the indexation are provided in the supplemental information (Table S2).

Among the advantages accompanying to thin film technology, one of the most appealing is the production of cost-effective materials, as the active material can be reduced to a minimum while the functionality is maintained. In this regard the sol properties (viscosity, surface tension, solid fraction) and operational parameters (substrate subtraction velocity) were tuned to afford nanometric coatings. Accordingly, the weight of titania ranged from a minimum of 11 $\mu g \cdot g^{-1}$ for PPC-20 and PPC-30, to a maximum of 16 $\mu g \cdot g^{-1}$ for PPC-0. The thickness and rugosity of the coatings were measured by mechanical profilometry (Table 3). The protective SiO_2 barrier, deposited on all substrates prior to titania coatings, is 258 nm thick. The mean thickness of PPC-0 was 58 nm, while the lowering of the sol viscosity and surface tension prompted by the addition of the ALS led to thinner coatings ranging from 31 to 35 nm. However, no significant differences were appreciated among the films containing different amounts of template. The coating surfaces are rather smooth with roughness values retained in all cases around 1–2 nm. Note that such low surface roughness values are desirable to reduce diffuse light scattering that might occur upon the UV irradiation at the photoreactor.

At this point, it is also convenient to assess the endurance of the thin films in order to assure a long-term stability. Accordingly, the adhesion of the coating to the substrate was checked by cross-cut test. All samples showed good adhesion and did not show any delamination. Figure S3 shows microscope images before and after the test, where it can be seen the coating perfectly maintains its integrity.

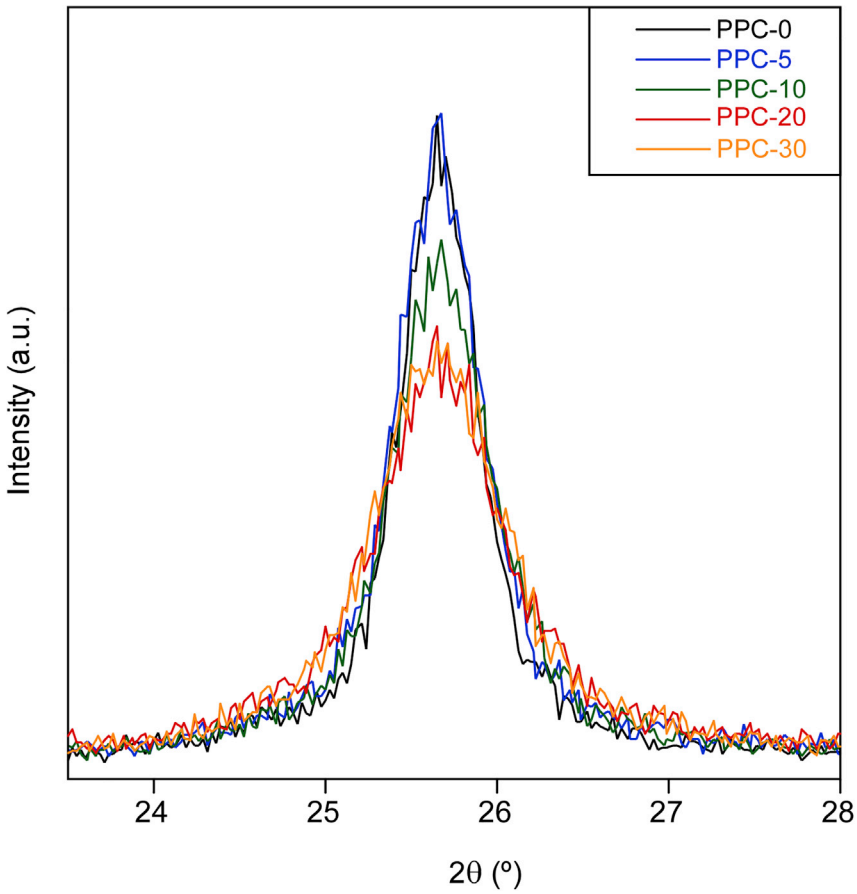

Figure 2. PXRD showing the widening of (101) reflection

Table 4 gathers the specific surface area, pore size and porosity estimated for each sample from N_2 adsorption isotherms (Figure S4). All of them exhibited type IV adsorption-desorption isotherms with an elongated S-type hysteresis loop that indicates the mesoporous nature of the films. According to the pore size distribution analysis, all them show pores comprised within 3 and 12 nm, which are enough to ensure an agile diffusion of the chemical species through the pore network during their catalytic conversion. Apparently, no meaningful differences were appreciated in the pore distribution of the samples. Contrarily, surface area and porosity of the coatings increased gradually with template content of the sols, from minimum values of 14 m^2g^{-1} and 8% in absence of ALS to 78 m^2g^{-1} and 25% when 20% of ALS was incorporated. Further increase of the surfactant raised somewhat the porosity but worsened the surface area. It deserves to note that the trend described for the specific surface area is inversely related to the crystallite size (Table 2). In any case, the sintering occurring during the thermal treatment disables a direct comparison among both values.

Table 2. FWHM and crystallite sizes

Code	FWHM (°)	$D_{crystallite}$ (nm)
PPC-0	0.495	16.4
PPC-5	0.528	15.4
PPC-10	0.657	12.4
PPC-20	0.751	10.8
PPC-30	0.861	9.5

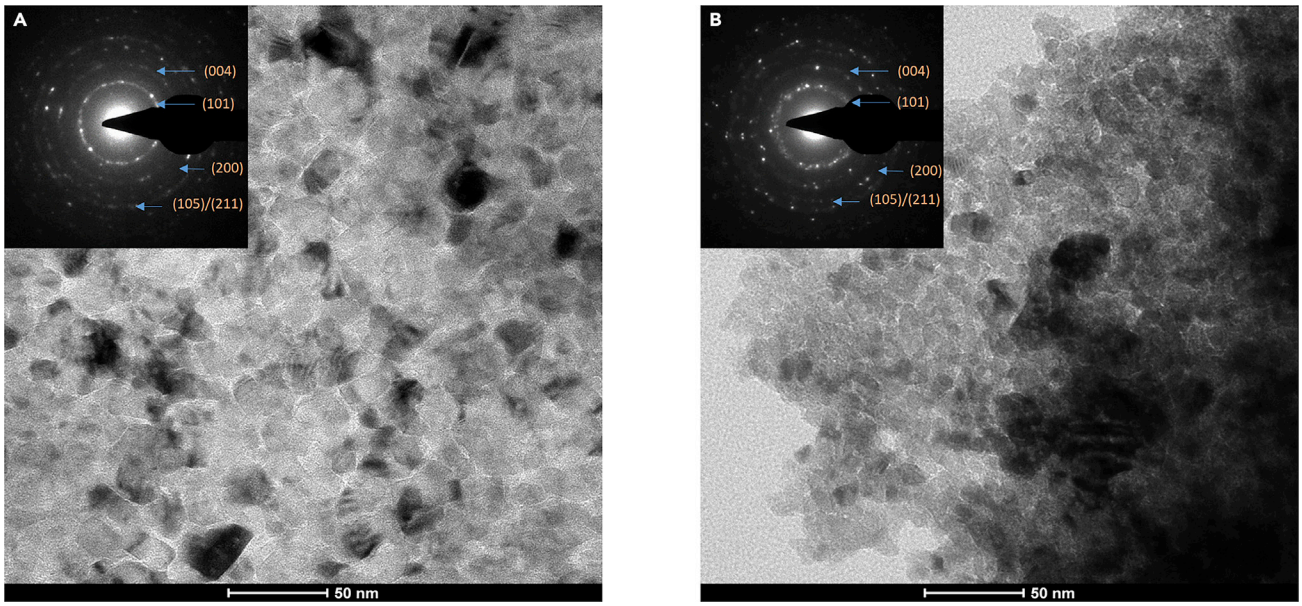

Figure 3. Lamellas TEM micrographs and SAED pattern showing the indexation of the diffraction rings (inset graphic)
(A and B) (A) PPC-0 and (B) PPC-20.

All in all, the analysis of the porosity features allows to point PPC-20 as the most promising window since it brings together the photocatalytic activity of nanosized anatase domains with a high surface area and porosity that can boost the reaction kinetics.

Optical behavior and preliminary photoactivity

Figure 4 compares the transmittance and absorbance spectra of neat glass substrate with those of coated with SiO_2 barrier and photocatalytic films. Due to multiple beam interference the SiO_2 film increases the transmittance by *ca.* 3% near to the absorption edge of TiO_2 which in principle provides the capability to increase the amount of photons with suitable energy reaching the catalytic layer. The glasses containing the photocatalytic films exhibit transmittance values somewhat lower in the visible region due to the increase of the reflectance (Figure S5) that results from the higher refractive index of the titania with respect to the silica barrier and glass. However, the sudden decrease taking place at lower wavelengths is attributable to the absorption edge of the TiO_2 films, in concordance with the absorbance spectra.

The optical band gap values of semiconductor films were estimated from the Tauc formula (see supplemental information) (Tauc et al., 1966; Makuta et al., 2018). The linear regression $(\alpha h\nu)^{0.5}$ vs $h\nu$ plots at absorption edge yielded optical band-gap values ranging from 3.17 to 3.20 eV (Figure 5). These values are comparable to that expected for anatase bulk phase (3.2 eV) (Luttrell et al., 2015).

Table 3. Thin film thickness and roughness values.

Sample	L_{exp} (nm)[a]	R_a (nm)[b]
B-SiO_2	258 (9)	0.69
PPC-0	58 (9)	1.14
PPC-5	33 (7)	0.70
PPC-10	31 (3)	0.87
PPC-20	32 (3)	1.83
PPC-30	35 (5)	1.36

[a]L_{exp}: measured film thickness.
[b]R_a: arithmetical surface roughness.

Table 4. Pore size, surface area, and porosity values.

Code	D_{mode} (nm)	D_{range} (nm)	BET ($m^2 \cdot g^{-1}$)	Porosity (%)
PPC-0	5.5	4.0–11.2	14.4	7.9
PPC-5	6.8	3.6–11.6	29.9	14.1
PPC-10	6.3	3.6–9.8	43.5	18.4
PPC-20	5.4	2.8–8.1	78.1	23.1
PPC-30	5.9	3.5–8.4	73.4	25.3

Compared to PPC-0, the lowering of the E_g value taking place in PPC-5, -10, −20 and −30 can be attributed to the small amounts of S and N detected by XPS analysis (Figure S9) and that results from the use of ALS template in the sols. Compared to the O 2p orbital, N and S have 2p orbitals with less negative energy levels and thus, a partial substitution of the lattice O by N or S dopants leads to new energy bands above the TiO_2 valence band, reducing as consequence the effective band gap (Schneider et al., 2014; Serpone, 2006; Cai et al., 2020). It deserves to note that the band gap energy of PPC-20 and PPC-30 tend to increase which can be ascribed to the size dependent quantization of titania, that in fact tend to be more marked below 10 nm (Linsebigler et al., 1995; Serpone et al., 1995; Almquist and Biswas, 2002). Despite it has been demonstrated that non-metal element doping into TiO_2 promotes a redshift of the light absorption to lower energies, it is still controversial if this doping is beneficial to the photocatalytic process (Bakar and Ribiro, 2016).

To assess the preliminary photoactivity of the coatings, the photodegradation of Remazol Black B was studied. The photocatalytic pigment degradation provides a straightforward tool to preliminarily estimate the performance of the windows prior to assemble them into the optofluidic microreactor. Figure 6 shows the time evolution of relative dye concentration (C/C_o where C and C_o represent dye concentration at a particular time and initial concentration, respectively). For comparative purposes the reaction times have been limited to 2 hr, but prolonged irradiations (22 hr) have shown a quantitative degradation of the dye (Figure S6).

Photocatalytic degradation kinetic of Remazol Black B fits to a first-order reaction (Houas et al., 2001). Calculated rate constants and half-life values are gathered in Table 5, while fitting the experimental data is shown in Figure S7.

As mentioned in the introductory section, the protective SiO_2 layer pursues to prevent the poisoning caused by the diffusion of sodium ions during the thermal treatment. In this sense, Figure 6 compares the photocatalytic response of two windows with and without the protective silica layer (PPC-0 and PPC-0*, respectively). It becomes clear that in absence of the silica barrier, the photocatalytic layer is inactive,

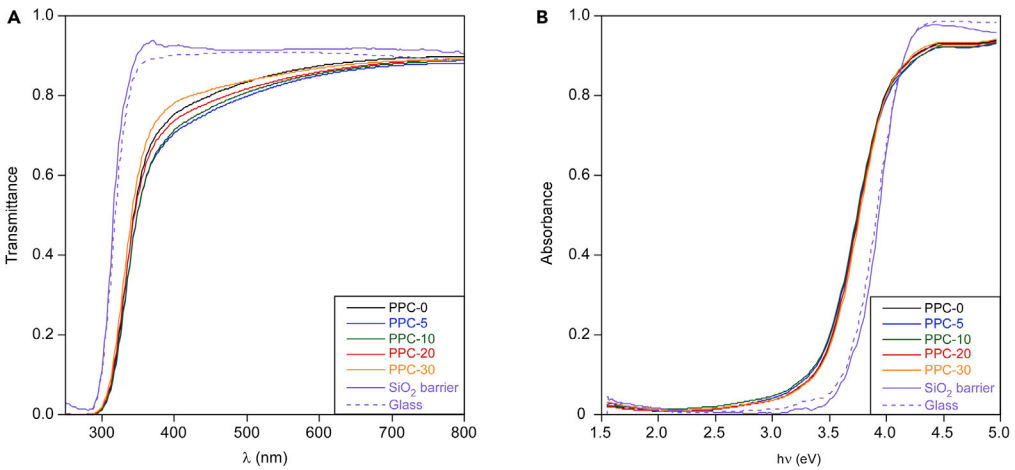

Figure 4. Spectra for neat glass and glass coated with silica barrier and photocatalytic films
(A and B) (A) Transmittance and (B) absorbance.

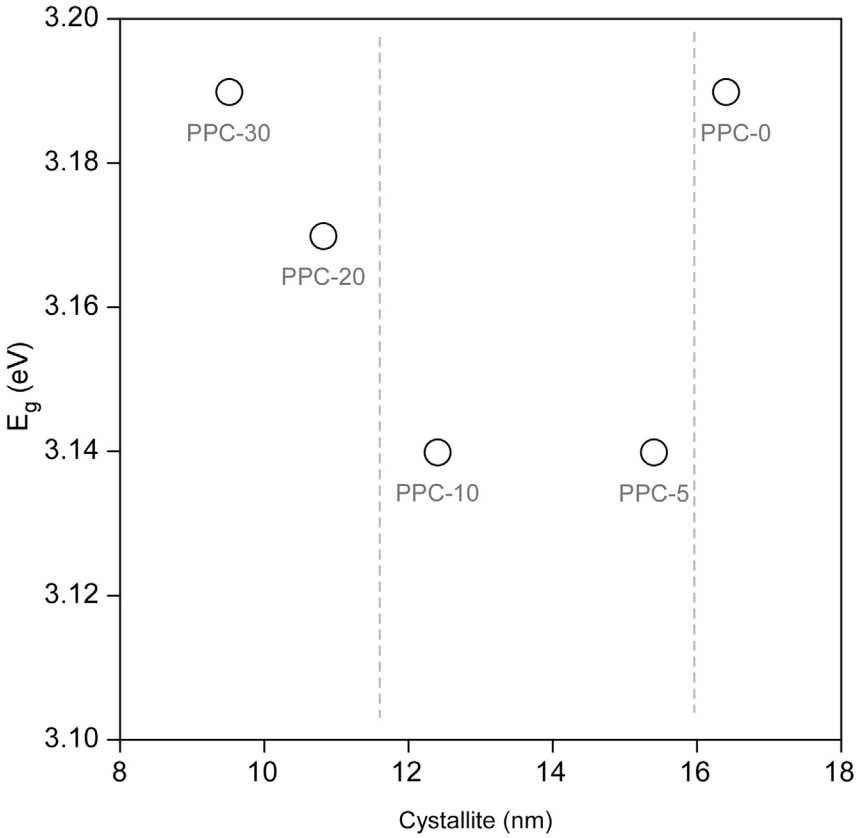

Figure 5. Band gap energy (E_g) vs crystallite size
From right to left, the dashed lines represent the redshift and blueshift attributed to N and S content and size quantization, respectively.

while the pre-coated DPC sample shows a meaningful response that degrades 36% of the dye upon 2 hr of illumination.

Regarding the influence of microstructural features of the coatings (Tables 2 and 3) in the photoactivity, PPC-5 shows a similar performance to that of PPC-0. Note that despite the former presents somewhat greater surface area and porosity, and both have similar crystallite size. Contrarily, the more noteworthy crystallite size reduction and porosity increase detailed for PPC-10 and PPC-20 seems to be the responsible for the photodegradation performance improvement they exhibit. Unexpectedly, PPC-30 presents a slightly smaller rate constant than PPC-20, despite of exhibiting similar microstructural features. Such photoactivity decay can be ascribed to counterproductive effect of the increase of N and S content in PPC-30, that exceed that of PPC-20 (Figure S9).

Continuous transformation of CO_2 in a planar optofluidic microreactor

The developed photoactive windows (10 × 10 mm^2; thickness: 3.8 mm) were assembled in a planar optofluidic microreactor for the continuous transformation of CO_2 (APRIA Systems S.L.) (Figure 7). The materials were placed in a 1 cm^2 reaction microchamber (75 μL) and irradiated with 1200 mW (365 nm) LED light with an intensity of E = 10 $mW \cdot cm^{-2}$ measured by a radiometer (Photoradiometer Delta OHM). The material was sandwiched with PTFE gaskets between two highly transparent (light transmission of 90% at >365 nm) polymethylmethacrylate, PMMA (Altuglas-Arkema) plates and a stainless-steel plate on the top. The photocatalytic windows were placed in the center of the reaction chamber of the PMMA plate, as represented in Figure 7, and the reactor was operated in a one-compartment configuration. A full description of the experimental setup and reactor details can be found elsewhere (Albo et al., 2021), while details on the reagent flux and chemical analysis are detailed in the experimental procedures section.

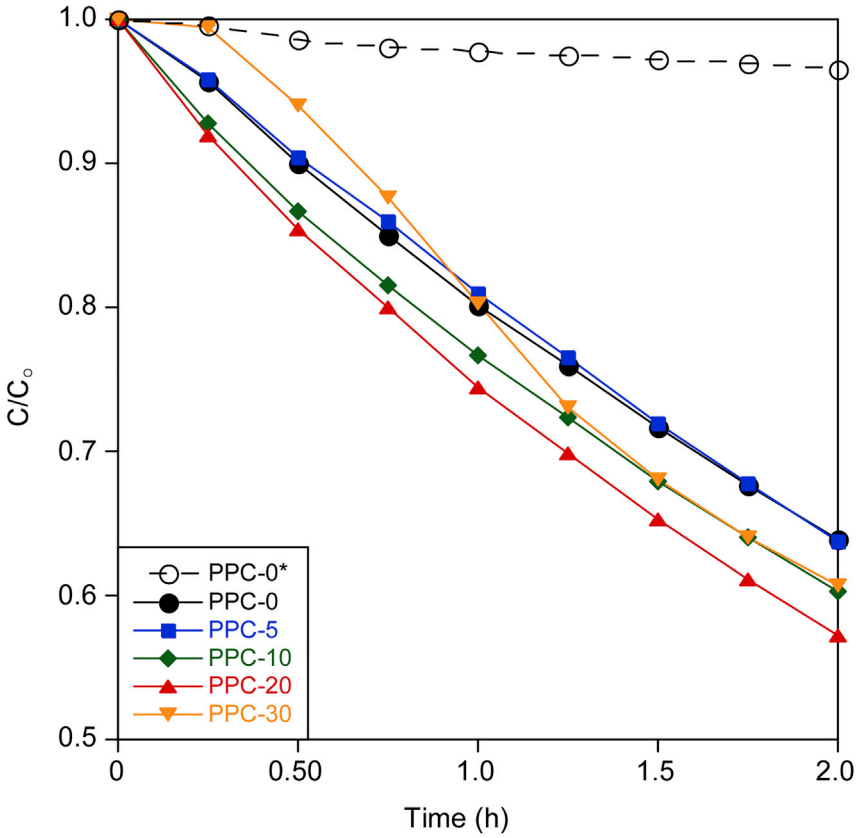

Figure 6. Evolution of the relative dye concentration for the photocatalytic coatings
PPC-0* lacks of silica barrier.

The results (*r* and *AQY*) for the continuous photoreduction of CO_2 with the fabricated photocatalytic windows with different ALS content in the sol (0–30%) are shown in Table 6. The system led to the formation of methanol, with also trace amounts of HCOOH, which is a probable intermediate in the CO_2-to-methanol reaction (Albo et al., 2019). Gas-phase products were not analyzed. It should be also noted that blank tests were also conducted in the dark and the absence of CO_2 and no CO_2-reduction liquid-phase products were detected.

The data firstly show that the yields for methanol are increased for the photocatalytic windows prepared from sols containing 5–20% of ALS (PPC-5, PPC-10, and PPC-20), which can be related to the crystallite size reduction and porosity increase of the anatase coatings (Tables 2 and 3). Contrarily to the afore discussed batch photodegradation tests (Table 5), the continuous flow CO_2 photoreduction reaction seems to be more sensitive to porosity increase, as the performance is markedly improved even in PPC-5. The optimal point is achieved for PPC-20 in which the production of methanol is as high as r = 0.52 $\mu mol \cdot h^{-1} \cdot cm^{-2}$ (*AQY* = 2.84%) after 2 hr of UV illumination. It also worth mentioning that the

Table 5. Dye photocatalytic decomposition in 2 hr (R), rate constants (K_1) and half-life (T_{50}) values.

Code	R (%)	K (h^{-1})	T_{50} (h)
PPC-0	36.17	0.222	3.12
PPC-5	36.25	0.219	3.15
PPC-10	39.69	0.257	2.69
PPC-20	42.78	0.284	2.43
PPC-30	39.25	0.245	2.83

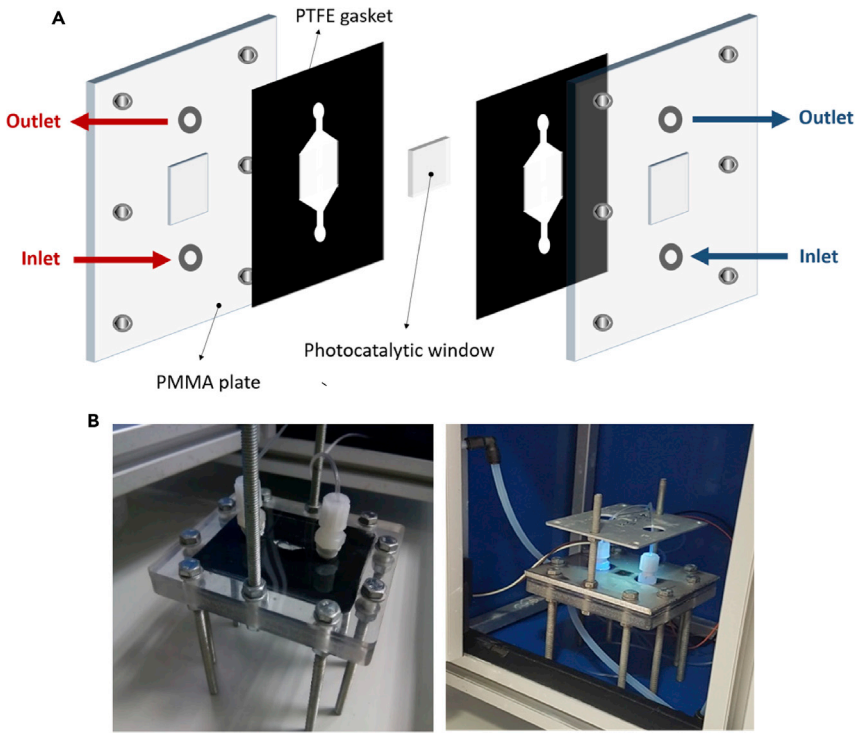

Figure 7. Reactor design for the photocatalytic CO_2 conversion
(A and B) (A) Inner parts, and (B) images of the micro-optofluidic reactor.

production rate and efficiency are higher than the values achieved before over bare TiO_2 (P25) (Albo et al., 2021), Cu/TiO_2 (Albo et al., 2021) or Mo_2C/TiO_2 (Albo and García. 2021) in the same optofluidic microreactor illuminated with UV (Table S3 in supplemental information) but with a remarkably higher catalyst loading (2 mg·cm^{-2}), which further denotes the benefits of the nanometric photocatalyst films developed (ca. 11 μg·cm^{-2} for PPC-20). This minimum active material required is far from the mg·cm^{-2} level in other TiO_2-based microreactor systems (Cheng et al., 2016, 2017a). Moreover, PPC-30 shows a slight worsening in the formation of methanol with respect to PPC-20, despite of their comparable values of surface area and crystallite size. As mentioned in the preliminary assessment of the photocatalytic performance, such decay can be related to the counterproductive effect of the increase of N and S content in PPC-30 with regard to PPC-20.

Furthermore, Figure 8A shows the yields for methanol obtained with PPC-20 at longer irradiation times, while Figure 8B shows the rates after two consecutive runs.

As it can be observed, the activity of the photocatalytic windows can be still slightly enhanced up to 4 hr of irradiation, going to r = 0.55 μmol·h^{-1}·cm^{-2} and AQY = 3.02%. This behavior can be linked to the removal of the N and S excess from the surface of the particles which, in fact, it has been checked by

Table 6. Performance for the photoreduction of CO_2 with the photoactive windows.

Material	r_{CH3OH} (μmol·h^{-1}·cm^{-2})	AQY (%)
PPC-0	0.28	1.51
PPC-5	0.39	2.15
PPC-10	0.51	2.76
PPC-20	0.52	2.84
PPC-30	0.45	2.48

Q_L = 125 μL·min^{-1} and E = 10 mW·cm^{-2} (UV).

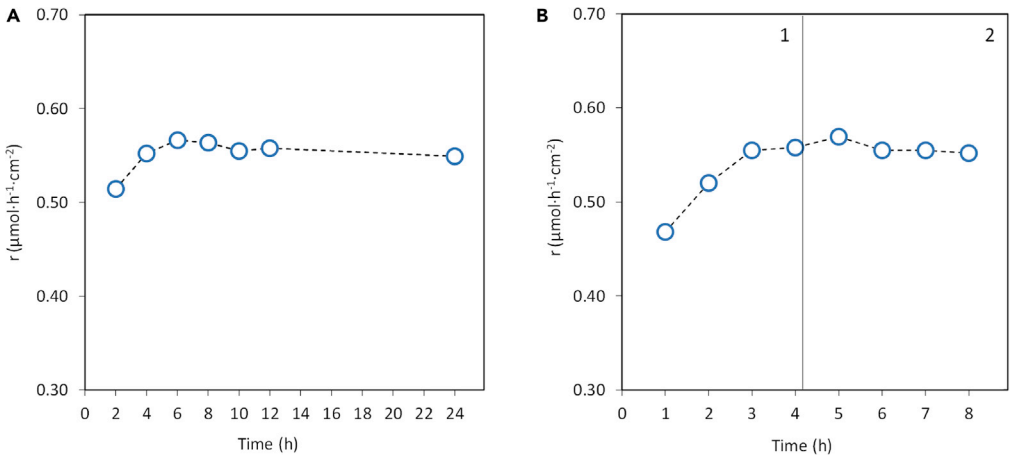

Figure 8. Photocatalytic production of methanol using PPC-20
(A and B) (A) Time-dependence for 24 h (B) two-consecutive runs

the post-reaction XPS analysis of the photocatalytic windows (Figure S10). Beyond this point, the performance remains almost invariable after 24 hr of continuous operation and after two consecutive runs, which means the material keeps its photocatalytic ability with time in contrast to common photocatalysts applied in CO_2 conversion (Meister et al., 2015). Overall, the results reveal the potential of the developed photoactive windows for stable production of methanol under UV light, although research needs to continue to bring productivity values closer to real applications.

Conclusions

The setting of the TiO_2 sol formulation and processing conditions allowed us to generate five photocatalytic windows based on anatase nanometric coatings (30–60 nm) with controlled crystallite size, porosity, and thickness. The band gap of the coatings was close to 3.2 eV, as expected for anatase, despite slight redshift and blueshift were observed, ascribable, respectively, to minor content of C, N, and S and to size quantization phenomena in those coatings with the smallest crystallites (9–10 nm). Apart from that, it has been found that pigment photodegradation experiments can be regarded as a straightforward preliminary test due their good correlation with CO_2 photoreduction results.

Regarding the performance of the continuous flow optofluidic microreactor, the porosity and crystallite size of the coatings are transcending parameters which allowed us to optimize the reaction rate and the yield. It must be emphasized that under optimum conditions the performance of the photocatalytic windows surpassed that provided by supported benchmark TiO_2 nanoparticle (P25) and does not decay within 8 hr of operation as the robustness of the coating prevents any leaching of the photocatalytic material. Another meaningful advantage relies in the nanometric thickness of the photocatalytic films since it allows the production of cost-effective materials by reducing the active material to a minimum (*ca.* 11 $\mu g \cdot cm^{-2}$).

All in all, the herein reported photocatalytic windows simplify the design and operation of the optofluidic microreactor, providing a competitive performance respect common supported catalyst approach. Nonetheless, further work is still needed to get productivity values closer from the industrial demands. In this sense, processing as photocatalytic window high efficiency materials (Wang et al., 2020; Wei et al., 2018; Wu et al., 2019; He et al., 2020) could be a next appealing challenge to invigorate further the performance of optofluidic microreactors.

Limitations of study

The herein presented study demonstrates how the design of an optofluidic microreactor can be simplified by the use of a photocatalytic window based on nanostructured TiO_2 coating, providing also a more straightforward operation and higher performance of the photoreduction of CO_2 into methanol. However, the study lacks of the quantification of gaseous products (CO, CH_4…) whose production can be also

meaningful. In this regard, the analysis of both liquid and gas fraction of the reaction would offer a more detailed view of the overall process.

STAR★METHODS

Detailed methods are provided in the online version of this paper and include the following:

- KEY RESOURCES TABLE
- RESOURCE AVAILABILITY
  - Lead contact
  - Materials availability
  - Data and code availability
- METHODS DETAILS
  - Preparation of photocatalytic windows
  - Physical measurements
  - Photocatalytic degradation experiments
  - Photoreduction of CO_2 in an optofluidic microreactor

SUPPLEMENTAL INFORMATION

Supplemental information can be found online at https://doi.org/10.1016/j.isci.2021.102654.

ACKNOWLEDGMENTS

The authors gratefully acknowledge the financial support from the Basque Government (PIBA18/14; IT1291-19), the Spanish Ministry of Science and Innovation (MICINN projects: PID2019-104050RA-I00 and PID2019-108028GB-C21), the European Union's Horizon 2020 research and innovation program (grant agreement No 792103 SOLWARIS) and the Ramón y Cajal programme (RYC-2015-17080). Technical and human support provided by SGIker (UPV/EHU, MICINN, GV/EJ, and ESF) is also acknowledged.

AUTHOR CONTRIBUTIONS

Conceptualization, G.B. and J.A.; funding acquisition, J.A., E.A., and O.C.; investigation, A.A.-I., A.M.G., J.A., E.A., G.B., O.C., and S.P.-Y.; methodology, A.M.G., G.B. and S.P.-Y.; resources, J.A., E.A. and O.C.; supervision, A.M.G., E.A. and G.B.; writing – original draft, J.A. and G.B.; writing – review & editing A.A.-I., A.M.G., J.A., E.A., G.B., O.C. and S.P.-Y.

DECLARATION OF INTERESTS

The authors declare no competing interests.

Received: February 22, 2021
Revised: April 23, 2021
Accepted: May 24, 2021
Published: June 25, 2021

REFERENCES

Albo, J., and García, G. (2021). Enhanced visible-light photoreduction of CO2 to methanol over Mo2C/TiO2 surfaces in an optofluidic microreactor. React. Chem. Eng. *6*, 304–312.

Albo, J., Perfecto-Irigaray, M., Beobide, G., and Irabien, A. (2019). Cu/Bi metal-organic framework-based systems for an enhanced electrochemical transformation of CO2 to alcohols. J. CO2 Util. *33*, 157–165.

Albo, J., Qadir, M.I., Samperi, M., Fernandes, J.A., de Pedro, I., and Dupont, J. (2021). Use of an optofluidic microreactor and Cu nanoparticles synthesized in ionic liquid and embedded in TiO2 for an efficient photoreduction of CO2 to methanol. Chem. Eng. J. *404*, 126643.

Almquist, C.B., and Biswas, P. (2002). Role of synthesis method and particle size of nanostructured TiO2 on its photoactivity. J. Catal. *212*, 145–156.

Bakar, S.A., and Ribeiro, C. (2016). Nitrogen-doped titanium dioxide: an overview of material design and dimensionality effect over modern applications. J. Photochem. Photobiol. C Photochem. Rev. *27*, 1–29.

Cai, J., Shen, F., Shi, Z., Lai, Y., and Sun, J. (2020). Nanostructured TiO2 for light-driven CO2 conversion into solar fuels. APL Mater. *8*, 40914.

Chen, R., Cheng, X., Zhu, X., Liao, Q., An, L., Ye, D., He, X., and Wang, Z. (2017). High-performance optofluidic membrane microreactor with a mesoporous CdS/TiO2/SBA-15@carbon paper composite membrane for the CO2 photoreduction. Chem. Eng. J. *316*, 911–918.

Cheng, X., Chen, R., Zhu, X., Liao, Q., He, X., Li, S., and Li, L. (2016). Optofluidic membrane microreactor for photocatalytic reduction of CO2. Int. J. Hydrogen Energy *41*, 2457–2465.

Cheng, M., Yang, S., Chen, R., Zhu, X., Liao, Q., and Huang, Y. (2017a). Copper-decorated TiO2 nanorod thin films in optofluidic planar reactors for efficient photocatalytic reduction of CO2. Int. J. Hydrogen Energy *42*, 9722–9732.

Cheng, X., Chen, R., Zhu, X., Liao, Q., An, L., Ye, D., He, X., Li, S., and Li, L. (2017b). An optofluidic planar microreactor for photocatalytic reduction

of CO2 in alkaline environment. Energy *120*, 276–282.

Cheng, M., Huang, Y., Gao, R., and Bai, S. (2019). Numerical simulation of photocatalytic reduction of gas phase CO2 in optofluidic microreactor. Catal. Lett. *149*, 3000–3011.

Dijkstra, M.F.J., Michorius, A., Buwalda, H., Panneman, H.J., Winkelman, J.G.M., and Beenackers, A.A.C.M. (2001). Comparison of the efficiency of immobilized and suspended systems in photocatalytic degradation. Catal. Today *66*, 487–494.

Fujishima, A., and Rao, T.N. (1997). Recent advances in heterogeneous TiO2 photocatalysis. J. Chem. Sci. *109*, 471–486.

He, W., Wu, X., Li, Y., Xiong, J., Tang, Z., Wei, Y., Zhao, Z., Zhang, X., and Liu, J. (2020). Z-scheme heterojunction of SnS2-decorated 3DOM-SrTiO3 for selectively photocatalytic CO2 reduction into CH4. Chin. Chem. Lett. *31*, 2774–2778.

Holzwarth, U., and Gibson, N. (2011). The Scherrer equation versus the "Debye-Scherrer equation. Nat. Nanotechnol. *6*, 534.

Houas, A., Lachheb, H., Ksibi, M., Elaloui, E., Guillard, C., and Herrmann, J.M. (2001). Photocatalytic degradation pathway of methylene blue in water. Appl. Catal. B Environ. *31*, 145–157.

Khalaf, S., Shoqeir, J.H., Scrano, L., Karaman, R., and Bufo, S.A. (2019). Photodegradation using TiO2-activated borosilicate tubes. Environ. Sci. Pollut. Res. *26*, 19025–19034.

Klug, H.P., and Alexander, L.E. (1974). X-Ray Diffraction Procedures (Wiley).

Lee, K.S., and Lee, S.H. (2007). Influence of SiO2 interlayer on the hydrophilicity of TiO2/SiO2/ glass produced by RF-magnetron sputtering. Mater. Lett. *61*, 3516–3518.

Li, L., Tang, D., Song, Y., and Jiang, B. (2018). Dual-film optofluidic microreactor with enhanced light-harvesting for photocatalytic applications. Chem. Eng. J. *339*, 71–77.

Linsebigler, A.L., Lu, G., and Yates, J.T. (1995). Photocatalysis on TiO2 surfaces: principles, mechanisms, and selected results. Chem. Rev. *95*, 735–758.

Luttrell, T., Halpegamage, S., Tao, J., Kramer, A., Sutter, E., and Batzill, M. (2015). Why is anatase a better photocatalyst than rutile? - model studies on epitaxial TiO2 films. Sci. Rep. *4*, 4043.

Makuła, P., Pacia, M., and Macyk, W. (2018). How to correctly determine the band gap energy of modified semiconductor photocatalysts based on UV-vis spectra. J. Phys. Chem. Lett. *9*, 6814–6817.

Meister, S., Reithmeier, R.O., Tschurl, M., Heiz, U., and Rieger, B. (2015). Unraveling side reactions in the photocatalytic reduction of CO2: evidence for light-induced deactivation processes in homogeneous photocatalysis. ChemCatChem *7*, 690–697.

Nam, H.J., Amemiya, T., Murabayashi, M., and Itoh, K. (2004). Photocatalytic activity of Sol-Gel TiO2 thin films on various kinds of glass substrates: the effects of Na+ and primary particle size. J. Phys. Chem. B *108*, 8254–8259.

Novotna, P., Krysa, J., Maixner, J., Kluson, P., and Novak, P. (2010). Photocatalytic activity of sol-gel TiO2 thin films deposited on soda lime glass and soda lime glass precoated with a SiO2 layer. Surf. Coat. Technol. *204*, 2570–2575.

Ola, O., and Maroto-Valer, M.M. (2015). Review of material design and reactor engineering on TiO2 photocatalysis for CO2 reduction. J. Photochem. Photobiol. C Photochem. Rev. *24*, 16–42.

Ola, O., Maroto-Valer, M., Liu, D., MacKintosh, S., Lee, C.W., and Wu, J.C.S. (2012). Performance comparison of CO 2 conversion in slurry and monolith photoreactors using Pd and Rh-TiO 2 catalyst under ultraviolet irradiation. Appl. Catal. B Environ. *126*, 172–179.

Paz, Y., Luo, Z., Rabenberg, L., and Heller, A. (1995). Photooxidative self-cleaning transparent titanium dioxide films on glass. J. Mater. Res. *10*, 2842–2848.

Schneider, J., Matsuoka, M., Takeuchi, M., Zhang, J., Horiuchi, Y., Anpo, M., and Bahnemann, D.W. (2014). Understanding TiO2photocatalysis: mechanisms and materials. Chem. Rev. *114*, 9919–9986.

Serpone, N. (2006). Is the band gap of pristine TiO 2 Narrowed by anion-and cation-doping of titanium dioxide in second-generation photocatalysts? J. Phys. Chem. *110*, 24287–24293.

Serpone, N., Lawless, D., and Khairutdinov, R. (1995). Size effects on the photophysical properties of colloidal anatase TiO2 particles: size quantization or direct transitions in this indirect semiconductor? J. Phys. Chem. *99*, 16646–16654.

Shan, A.Y., Ghazi, T.I.M., and Rashid, S.A. (2010). Immobilisation of titanium dioxide onto supporting materials in heterogeneous photocatalysis: a review. Appl. Catal. A Gen. *389*, 1–8.

Sohrabi, S., Keshavarz Moraveji, M., and Iranshahi, D. (2020). A review on the design and development of photocatalyst synthesis and application in microfluidic reactors: challenges and opportunities. Rev. Chem. Eng. *36*, 687–722.

Tauc, J., Grigorovici, R., and Vancu, A. (1966). Optical properties and electronic structure of amorphous germanium. Phys. Status Solidi. *15*, 627–637.

Wang, N., Zhang, X., Wang, Y., Yu, W., and Chan, H.L.W. (2014). Microfluidic reactors for photocatalytic water purification. Lab Chip *14*, 1074–1082.

Wang, C., Zhao, Y., Xu, H., Li, Y., Wei, Y., Liu, J., and Zhao, Z. (2020). Efficient Z-scheme photocatalysts of ultrathin g-C3N4-wrapped Au/ TiO2-nanocrystals for enhanced visible-light-driven conversion of CO2 with H2O. Appl. Catal. B Environ. *263*, 118314.

Wei, Y., Wu, X., Zhao, Y., Wang, L., Zhao, Z., Huang, X., Liu, J., and Li, J. (2018). Efficient photocatalysts of TiO2 nanocrystals-supported PtRu alloy nanoparticles for CO2 reduction with H2O: synergistic effect of Pt-Ru. Appl. Catal. B Environ. *236*, 445–457.

Wu, X., Wang, C., Wei, Y., Xiong, J., Zhao, Y., Zhao, Z., Liu, J., and Li, J. (2019). Multifunctional photocatalysts of Pt-decorated 3DOM perovskite-type SrTiO3 with enhanced CO2 adsorption and photoelectron enrichment for selective CO2 reduction with H2O to CH4. J. Catal. *377*, 309–321.

STAR★METHODS

KEY RESOURCES TABLE

REAGENT or RESOURCE	SOURCE	IDENTIFIER
Chemicals, peptides, and recombinant proteins		
Tetraethyl orthosilicate 98%	Sigma-Aldrich	Cat#131903
Titanium butoxide 97%	Sigma-Aldrich	Cat#244112
Ammonium lauryl sulfate	Sigma-Aldrich	Cat# 681806
Critical commercial assays		
Planar optofluidic microreactor-based setup	Apria Systems S.L.	23-001411
Other		
Headspace gas chromatograph	Shimadzu	GCMS-QP2010
Ion Chromatography	Thermo Fisher Scientific	ICS 1100 Dionex
UV fluorescence lamps (6W, 800uW/cm2)	Vilver	VL-6.L

RESOURCE AVAILABILITY

Lead contact

Further information and requests for resources should be directed to and will be fulfilled by the lead contact, Garikoitz Beobide (garikoitz.beobide@ehu.eus).

Materials availability

All materials generated in this study are available from the lead contact without restriction.

Data and code availability

This study did not generate any data sets.

METHODS DETAILS

Preparation of photocatalytic windows

All coatings were deposited on soda-lime glass substrates by dip-coating method into inorganic sols. In all cases the immersion and extraction velocities were set to 200 $mm \cdot min^{-1}$. Prior to the deposition of the photocatalytic films, the glass substrates were coated with a protective layer of silicon dioxide. The SiO_2 sols were prepared using tetraethyl orthosilicate (TEOS, 98%) as a precursor. TEOS was dissolved in half of the total ethanol volume. Thereafter, nitric acid and water were mixed in the remaining ethanol volume and added dropwise under continuous stirring into the TEOS solution. The molar ratio of TEOS:EtOH:H_2O:HNO_3 was set 1:40:4:0.04. The sols were aged for 24 hr.

Two kinds of photocatalytic films were prepared using titanium butoxide (TNBT, 97%) as a precursor. TNBT was dissolved in half of the total ethanol volume. Thereafter, nitric acid, water and ammonium lauryl sulfate (ALS, 30% in H_2O) were mixed in the remaining ethanol volume and added dropwise under continuous stirring into the TNBT solution. The molar ratio of TNBT:EtOH:H_2O:HNO_3:ALS was set to 1:165:2:0.04:X, where X was varied from 0 to 0.11 (Table 1) with the aim of tuning the microstructural features of the photocatalytic porous coatings (PPC). Higher concentrations of ALS surfactant were found to provide unstable sols that tend to gel in few hours. In order to obtain optimum and reproducible photocatalytic performances, prior to proceed with coating of substrates the sols were aged for a minimum of 5 days. The sols were found to be stable at greater aging times, while shorter aging times provided coating with smaller but increasing photocatalytic activity (Figure S8). Aged sols were reusable for several weeks providing reproducible results.

All freshly coated substrates were first air dried and then annealed at 450°C for 2 hr using a heating rate of $7°C \cdot min^{-1}$.

Physical measurements

Electron transmission microscopy (TEM) analysis was performed on a high resolution Tecnai G2 20 Twin microscope. TEM images and selected area electron diffraction (SAED) patterns were taken on subtracted lamellas of the coatings. The thicknesses and roughness of the films were measured by mechanical profilometry (Veeco Dektak 8, Stylus Profiler, Bruker). Data acquisition consisted of 3 mm long scans with a vertical resolution of 0.1 nm. The adhesion of the coating to the substrate was performed by crosscut test according to ASTM D 3359-09e2 standard test. Accordingly, a square pattern of incisions separated by 10 mm were made on each coating, followed by the application and subsequent removal. The results were assessed by the optical microscopy.

The optical characterization and band gap determination of the coatings was perfomed on a UV/VIS/NIR Perkin Elmer Lambda 950 spectrophotometer equipped with an integrating sphere (150mm Int. Sphere). The spectra were measured over the range 250 to 800 nm with a resolution of 1 nm.

Powder X-ray diffraction (PXRD) patterns were collected on xerogel samples using a Phillips X'PERT powder diffractometer (Panalytical, Eindhoven, The Netherlands) with Cu-Kα radiation (λ = 1.54060 Å) over the range $5° < 2\theta < 70°$ with a step size of 0.02° and an acquisition time of 2 s per step at 25°C. Dinitrogen (77 K) physisorption data was recorded on outgassed xerogel samples (vacuum at 150°C for 12 h) with a Quantachrome Autosorb-iQ-MP (Quantachrome Instruments, Florida, United States). The pore size distribution was modeled by density functional theory (DFT) as implemented in ASiQwin program of Quantachrome (ASiQwin V5.21, October 2010). Powdered xerogel samples were prepared by following the same thermal treatment to that of the coatings.

Photocatalytic degradation experiments

Photocatalytic performance on the degradation of a dye was tested by immersing the coated substrates in a borosilicate glass reactor containing an aqueous solution (80 mL) of a textile dye (Remazol Black B) with an initial concentration of 16.5μM and pH ≈ 2. To irradiate the reaction media two UV fluorescence lamps (6W, 800uW/cm^2) with a maximum emission at 365 nm were placed at 1 cm from the sample. The irradiation time was extended for 2 h. The temperature of the solution was maintained at 38(1) oC. To shelter from outside lighting, the reactor was covered by a black box. UV/VIS optical absorption spectrometry (250 – 800 nm) was used to monitor dye degradation. Upon a prior calibration, the dye concentration was calculated from the peak maxima sited at 597 nm. Time evolution of the dye concentration was used to assess the performance and kinetic of each coating. Dye was not degraded in absence of illumination and photocatalyst, which shows that no adsorption phenomena occurs on the surface of the films. Furthermore, in absence of photocatalysts, the photolysis of the pigment did not take place, ruling out the influence of these phenomena on the results.

Photoreduction of CO_2 in an optofluidic microreactor

A CO_2 saturated 0.5 M $KHCO_3$ (Panreac >97%) aqueous solution was prepared with ultra-pure water (18.2 MΩ cm at 273 K, MilliQ Millipore system) and supplied to the microchamber with a peristaltic pump (Minipuls 3 Gilson) at a flow rate of QL= 125 μL·min^{-1}. The microcell was placed in a ventilated dark box and temperature was controlled with an infrared thermometer (~20°C). Liquid samples were taken every 30 min and for 120 min at microreactor outlet. The concentration of alcohols in each sample was analyzed by duplicate in a headspace gas chromatograph (GCMS-QP2010 Ultra Shimadzu) equipped with a flame ionization detector (FID). Additionally, formate ($HCOO^-$) concentration was analyzed in duplicate by Ion Chromatography (Dionex ICS 1100). An average concentration was obtained for each point from the performance of three replicates (experimental error of less than 12.3%). The performance is analyzed in terms of *r* (i.e., yield per material surface and time) and apparent quantum yield, *AQY*:

$$AQY\ (\%) = \frac{n_e}{n_p}\ x\ 100$$

where n_e is the rate of electrons transferred toward a certain product, calculated by multiplying the number of molecules evolved (mol) by the number of reacted electrons (i.e. 6 e−for CH_3OH and 2 e−for HCOOH) and the Avogadro's number (mol^{-1}); and n_p is the rate of incident photons on the surface, calculated by multiplying the power density of the incident light (W·m^{-2}) by the irradiation area (m^2), reaction time (s) and wavelength peak (m), divided by the Planck's constant (J·s^{-1}) multiplied by the speed of light (m·s^{-1}).